

Preparation of tank-like resin-derived porous carbon sphere for supercapacitor: The influence of KOH activator and activation temperature on structure and performance

Xin Cui, Yuchen Jiang, Zhifeng He, Zeyi Liu, Xiaoyang Yang, Jiafeng Wan, Yifu Liu, Fangwei Ma^{*}

Key Laboratory of Chemical Engineering Processes & Technology for High-efficiency Conversion (College of Heilongjiang Province), School of Chemistry and Material Science, Heilongjiang University, Harbin 150080, China

ARTICLE INFO

Keywords:

Resorcinol-melamine-formaldehyde resin
Porous carbon
Tank-like
Activation
Supercapacitor

ABSTRACT

The resorcinol-melamine-formaldehyde (RMF) resin as a promising carbon precursor has aroused wide public concern due to its low cost, high nitrogen content, and ease of industrial production. In this work, the tank-like resorcinol-melamine-formaldehyde (RMF) resin spheres are synthesized via the hydrothermal method with the F127 assisting, and tank-like porous carbon spheres (TPCSs) are further prepared by pre-carbonization and KOH treatment. The F127 is crucial in the formation of tank-like resin spheres and the influence of KOH dosage and activation temperature on morphology, particle size and structure-activity relationships for resin-based carbon spheres are explored in detail. The particle size of RMF resin and TPCSs-X-Y mainly locate at 1.75–2.75 μm and 1–1.8 μm , respectively. TPCSs-2-600 possesses a specific surface area of 1338 $\text{m}^2 \text{g}^{-1}$ and a high N content of 11.49 %. The specific surface area of resin-based carbon materials initially increases and then decreases with increasing KOH activator, which affects the specific capacitance in a similar trend. The rate performance of resin-based porous carbon materials gets better with increasing KOH dosage due to enhanced ion transport ability resulting from pore size getting larger. Increasing activation temperature enhances the specific surface area and pore size of the carbon electrode, but the specific capacitance reduces gradually in three-electrode system. The cycle stability of TPCSs-2-600 can be 87.8 % after 10,000 times charge-discharge cycles at 10 A g^{-1} in two-electrode system, and the symmetric supercapacitor assembled with TPCSs-2-700 electrode shows a good energy density of 6.68 Wh kg^{-1} with a power density of 484 W kg^{-1} in 6 M KOH aqueous electrolyte.

1. Introduction

At present, the over-utilization of fossil fuels has caused an ever-increasing energy shortage crisis and environmental pollution in the world [1–4]. Therefore, the new type of portable and sustainable energy storage devices has attracted wide attention from plenty of researchers [5–7]. Supercapacitors (SCs), as a novel device of energy storage device, have been expansively explored and implemented in various fields, it is because that SCs possess the merit of highly efficient, better invertibility, environmental friendliness, longer cycle life, higher power density and faster charging/discharging speed compared with conventional batteries [8–13]. For SC, the mechanism of electrochemical energy storage could be separated into electrochemical double-layer capacitors (EDLCs) and pseudo-capacitors [14,15]. The process of accumulation charge for

an electric double-layer capacitor via electrostatic action results in the adsorption/desorption of electrolyte ions at the surface of the electrode/electrolyte [16]. Compared to Pseudocapacitors, the EDLCs have outstanding cycling stability and first-class rate performance. In order to enhance the performance of carbon-based supercapacitors, tuning the shape/size of particles, fabricating proper pore structure, and introducing heteroatoms are effective approaches [17,18].

Porous carbon material has emerged as a promising supercapacitor electrode material because it displays various advantages of low cost, environmental friendliness, outstanding electrical conductivity and physical/chemical stability, and so on [18–20]. The performance of porous carbon-based supercapacitors is influenced by specific surface area, heteroatom content (or functional groups), pore structure, and others [21]. So far, numerous synthesis methods for porous carbon

^{*} Corresponding author.

E-mail address: fangwei_ma@hotmail.com (F. Ma).

<https://doi.org/10.1016/j.diamond.2023.110054>

Received 12 April 2023; Received in revised form 6 May 2023; Accepted 20 May 2023

Available online 26 May 2023

0925-9635/© 2023 Elsevier B.V. All rights reserved.

materials primarily embrace the hydrothermal method [22], hard template method [23], soft template method [24], the self-template method [25], chemical/physical activation method [26,27], and so on. These synthesis strategies play a crucial role in the assembly of carbon materials. On the other hand, the structure characteristic of porous carbon is determined by raw materials in the synthesis reaction. Recently, resorcinol-melamine-formaldehyde (RMF) resin-based porous carbon material has obtained wide attention. It is because RMF resin possesses many advantages including adjustable morphology and pore structure, low cost, and introduction of nitrogen heteroatoms. Almost all RMF resin exhibit sphere shape, which possesses the excellent characteristics of regular geometry, adjustable particle size and tunable porosity [28,29]. Consequently, it is worth designing and exploring RMF resin-based carbon materials with outstanding performance as supercapacitor electrode.

In 2011, Liu's group [30] first reported the synthesis of monodisperse RF resin polymeric compound spheres by the Stöber method (a preparation method for monodisperse silica particles). It is an extremely facile and versatile route for resorcinol-formaldehyde (RF) resin spheres, the size of regular geometry can be regulated from 200 to 1000 nm while regulating concentration for ammonia or RF precursor. Ma et al. [31] explored an unusual template-free method from melamine and formaldehyde to synthesize resin spheres, obtaining nitrogen-doped hollow carbon spheres by high-temperature calcination. Compared to solid carbon spheres, the structure of nitrogen-doped hollow carbon microspheres displayed outstanding performance for electrode material resulting from its properties of high specific surface area and fast charge diffusion and transport ability. Liang et al. [32] prepared monodisperse phenolic resin spheres via a classical one-pot approach and straightforwardly introduced sulfur element by carbonization and KOH activation, and it possessed an excellent specific capacitance of 321 F g^{-1} at 0.5 A g^{-1} . For Zhu et al. [33], monodisperse melamine-formaldehyde resin microspheres (MMRMs) with F127 triblock copolymers as the soft template was developed via the mild emulsion polymerization method. Wherein, surfactants modulated the size of MMRMs and improved the thermostability of MMRMs due to the strong acting force of hydrogen bonds between F127 and resin. The carbonization structure of MMRMs possessed special lamellar porous morphology and high specific surface area. Ma's group [34] reported the preparation of spindle-like resin-based mesoporous carbon spheres by the polymerization and assembly of resorcinol, melamine, formaldehyde (raw materials) and F127 (assembly agent). It showed high specific surface area and good specific capacitance. Consequently, utilizing resin as a precursor for porous carbon material to construct high-performance supercapacitors is worth exploring.

Herein, we have prepared tank-like RMF resin microspheres at the higher concentration resorcinol-melamine-formaldehyde resin solution with F127 as surfactant by hydrothermal approach on the basis of the lower concentration resin solution for obtaining spindle-like mesoporous resin nanospheres [34]. Subsequently, tank-like porous carbon spheres are obtained via carbonization and KOH treatment. These as-prepared tank-like resin spheres are with sizes of $1.75\text{--}2.75 \mu\text{m}$, and tank-like porous carbon spheres become smaller with sizes of $1\text{--}1.8 \mu\text{m}$ after activation and possess a high specific surface area ($1338\text{--}2149 \text{ m}^2 \text{ g}^{-1}$). We detailly discuss the influence of activation processes including KOH dosages and activation temperature on the structure-activity relationship. The total specific capacitance loss was only 12.2 % after 10,000 cycles at the current density of 10 A g^{-1} in the two-electrode system, and the assembled TPCSs-2-700 symmetric supercapacitor exhibits a high energy density of 6.68 Wh kg^{-1} with a power density of 484 W kg^{-1} .

2. Experimental section

2.1. Synthesis of materials

2.1.1. Materials

Triblock copolymer Pluronic F127, resorcinol, melamine, formaldehyde (37 wt%), potassium hydroxide (KOH), ethanol, ultrapure water. All of the above chemical agents are analytical pure without any further purification.

2.1.2. Preparation of resorcinol-melamine-formaldehyde (RMF) resin

The resorcinol-melamine-formaldehyde (RMF) resin was synthesized by hydrothermal method. Commonly, 1.375 g of resorcinol (R), 0.75 g of melamine (M), and 2 g of formaldehyde solution were slowly dissolved in 100 mL of ultrapure water in a three-necked flask. After stirring at 25°C for 30 min, the solution of F127 (2.25 g of F127 was dissolved in 50 mL ultrapure water) was added and the reaction was subsequently carried out at room temperature (25°C) for 2 h. Then, the obtained transparent aqueous solution was separated into two equal parts and moved into two Teflon-lined autoclaves with the volume of 100 mL and then hydrothermal treatment at 130°C for 12 h. After naturally cooling to room temperature, the suspension was precipitated by centrifuge and then obtained sediment in brick red. The brick red precipitate was washed with ultrapure water and ethanol several times and was dried at 80°C for 12 h.

2.1.3. Preparation of resin-based carbon materials

In order to prepare carbon material, the RMF resin was firstly calcined at 600°C for 1 h in a tube furnace under a flow rate of $40\text{--}60 \text{ mL min}^{-1}$ ultrapure N_2 atmosphere. The obtained samples were labeled as TPCSs. The yield of TPCSs reaches around 33 % after the carbonization of RMF resin. After that, the resin-based carbon powder was uniformly mixed with KOH solid at room temperature for 30 min, the activation process was carried out for 2 h at different temperatures with a heating rate of 5°C min^{-1} under ultrapure N_2 atmosphere with a flow rate of 60 mL min^{-1} . Then, 10 M HCl solution and ultrapure water were used to remove residual KOH, followed by washing with ultra-pure water and ethanol several times until the pH value of the solution is about 7 and dried at 120°C for 12 h to obtain active carbon material. The obtained carbon samples were named TPCSs-X-Y (X = 1, 2 or 3, represents the weight ratio of KOH to carbon; Y is 600, 700, or 800°C , representing activation temperature). Besides, an identical procedure was followed for PCSs-2-600 but not adding F127 in the resin synthesis process. Moreover, 1.5 g of RMF resin and 0.5 g of KOH were dispersed and dissolved in a small amount of ultrapure water to obtain a slurry mixture. The obtained slurry mixture was dried at 80°C , and the activation process was carried out at 700°C for 2 h with a heating rate of 5°C min^{-1} under a flow rate of 60 mL min^{-1} ultrapure N_2 atmosphere. This carbon sample was collected and denoted as FPC-1-700.

2.2. Characterization

The morphologies of materials were checked by scanning electron microscope (SEM, Hitachi S-4800) and transmission electron microscope (TEM, JEOL JEM-2010), respectively. The X-ray diffraction (XRD) patterns of samples were collected on Rigaku D/max-IIIb with copper radiation ($\text{CuK}\alpha$, 0.15406 nm). The nitrogen adsorption and desorption isotherms were obtained at -196°C with a Quadachrome AUTOSORB-1-MP Adsorption Instrument. Brunauer-Emmett-Teller approach was utilized to calculate the specific surface area of carbon materials and the pore size distribution was measured by Density Functional Theory (DFT) method for as-prepared samples based on the N_2 isotherm desorption data. The Raman spectrum was recorded on the Jobin Yvon HR800 micro-Raman spectrometer with an excitation laser of 458 nm . The surface element composition of electrode material was performed by X-ray photoelectron spectroscopy (XPS) using VG ESCALAB MK II

(VGScientific, UK).

2.3. Electrochemical measurements

Firstly, the working electrode was obtained by compressing mixtures of active materials, carbon black (conductive agent), and polytetrafluoroethylene (PTFE, 2.5 %) binder with a weight ratio of 8:1:1 to form a slurry mixture. Next, the paste slurry was dried in an oven at 120 °C for 2 h, then 3 mg of the dried mixture of electrode material was loaded on a nickel foam current collector ($1 \times 1 \text{ cm}^2$), and Ni foam was pressed under a pressure of 8 MPa. Finally, The electrochemical performance was measured by the CHI760E electrochemical workstation (Chenhua, Shanghai, China) in the three-electrode and two-electrode systems in 6 M KOH.

Regarding electrochemical behaviors (three-electrode system), the platinum foil ($1 \times 1 \text{ cm}^2$) and Hg/HgO electrode were used as counter electrode and reference electrode, respectively. The cyclic voltammetry (CV) and galvanostatic charge/discharge (GCD) measurements were tested in potential windows of -1.0 to 0 V in 6 M KOH electrolyte. And the spectra of electrochemical impedance spectroscopy (EIS) measurement were obtained in the amplitude of 5 mV with the frequency range of 10 mHz to 100 kHz. The specific capacitance (C_s) was counted according to the following formula:

$$C_s = \frac{I\Delta t}{m\Delta V} \quad (1)$$

where I (A) and m (g) are the charge/discharge current and the mass of electroactive material in electrochemical measurements, respectively; Δt (s) and ΔV (V) are discharge time and potential windows that deduct the IR drop of the potential range.

For the two-electrode system, the electrochemical performance of the symmetrical supercapacitor was performed in 6 M KOH aqueous electrolyte. The CV and GCD measurements were tested in potential windows from 0 V to 1.0 V. The specific gravimetric capacitance for the single electrode in two-electrode system was calculated according to the following equation:

$$C_s = \frac{4I\Delta t}{m\Delta V} \quad (2)$$

where I (A) and m (g) are the charge/discharge current and the total mass of electroactive material in two-electrodes system, respectively; Δt (s) and ΔV (V) are discharge time and potential windows that deduct the IR drop of the voltage range.

The calculation of energy density and power density for a symmetrical supercapacitor is based on the following equations:

$$E_t = \frac{C_t(\Delta V)^2}{2 \times 3.6} \quad (3)$$

$$P_t = \frac{E_t}{\Delta t} \times 3600 \quad (4)$$

where E_t (Wh kg^{-1}) is the specific energy density, P_t (W kg^{-1}) is the specific power density, C_t (F g^{-1}) is the specific capacitance of symmetrical supercapacitor, Δt (s) and ΔV (V) are discharge time and potential windows that deduct the IR drop of the voltage range.

3. Results and discussion

3.1. Morphology and structural characterization

The preparation process of tank-like porous carbon microspheres is depicted in Fig. 1. Firstly, the tank-like resorcinol-melamine-formaldehyde (RMF) resin spheres were obtained via the hydrothermal method with the assistance of F127. Secondly, the as-prepared resin was calcinated at 600 °C in a tubular furnace. Finally, the tank-like carbon spheres and KOH were mixed excellently in mortar, and then the mixture was activated in a tube furnace. The possible mechanism of the tank-like resin sphere formation can be reported to illustrate as follows. Tank-like RMF resin was obtained by cross-linking and polycondensation reaction under the condition of hydrothermal treatment [31,35], and then the compound are gradually formed into polymer spheres to diminish surface energy after additional cross-linking and condensation [36]. Interestingly, other literature has mentioned a similar combination mode. For instance, Chen et al. used urea-phenol-formaldehyde resols precursors to react with F127 to prepare mesoporous spherical particles by hydrogen bonding [36]. Wang et al. designed a viable and effective method by one-step in situ pyrolysis of the crosslinking polymer melamine-formaldehyde-thiourea resins [35].

The morphologies of all as-synthesized carbon materials were characterized by scanning electron microscopy (SEM). The RMF resin possesses the morphology of tank-like microspheres and there is obvious arris in the edge, which is the combinative morphology of a cylinder in the middle and ellipsoidal head on two sides (Fig. S1a). The particle size of RMF resin spheres mainly focused on 1.75–2.75 μm (Fig. S1a). In Fig. 2a, TPCSs still retains tank-like microspheres morphology with smooth surface and devoid pores after the carbonization of RMF resin, but the particle size of as-prepared TPCSs is about 1–1.8 μm (Fig. S1b) with a whole diminution of about 40 % compared with RMF resin spheres due to the shrinkage happened with thermal decomposition. To further improve the specific surface area of TPCSs, the TPCSs have been activated by KOH at different temperatures and mass ratios of KOH to carbon. The inverted convex type surrounded by red line displays carbon samples prepared at different activation temperatures (600, 700, and 800 °C) and amounts of KOH. As shown in Fig. 2b, TPCSs-2-600 still possesses tank-like microspheres morphology, and the high-resolution SEM (HRSEM) image of TPCSs-2-600 further proves that the morphology is not microspheres but tank-like microspheres (Fig. 2c). To explore the influence of activation temperature on TPCSs structure, the

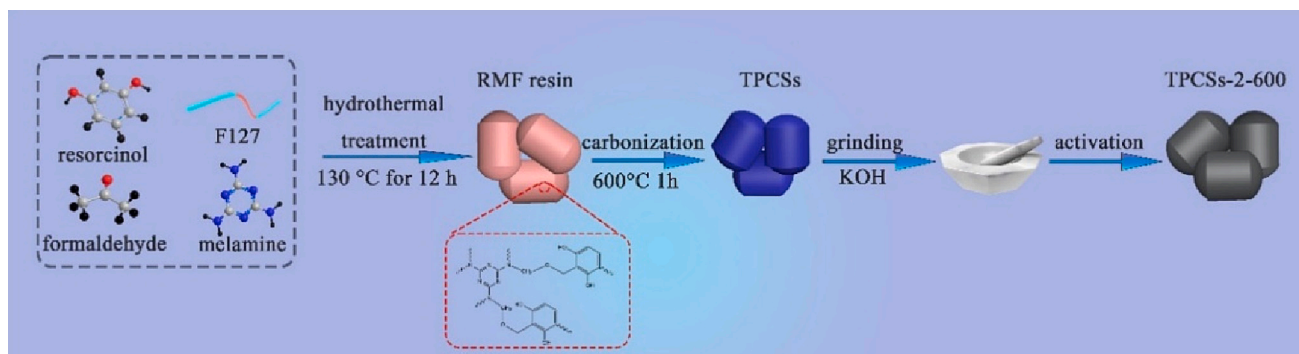


Fig. 1. Schematic illustration of tank-like resin-based carbon spheres.

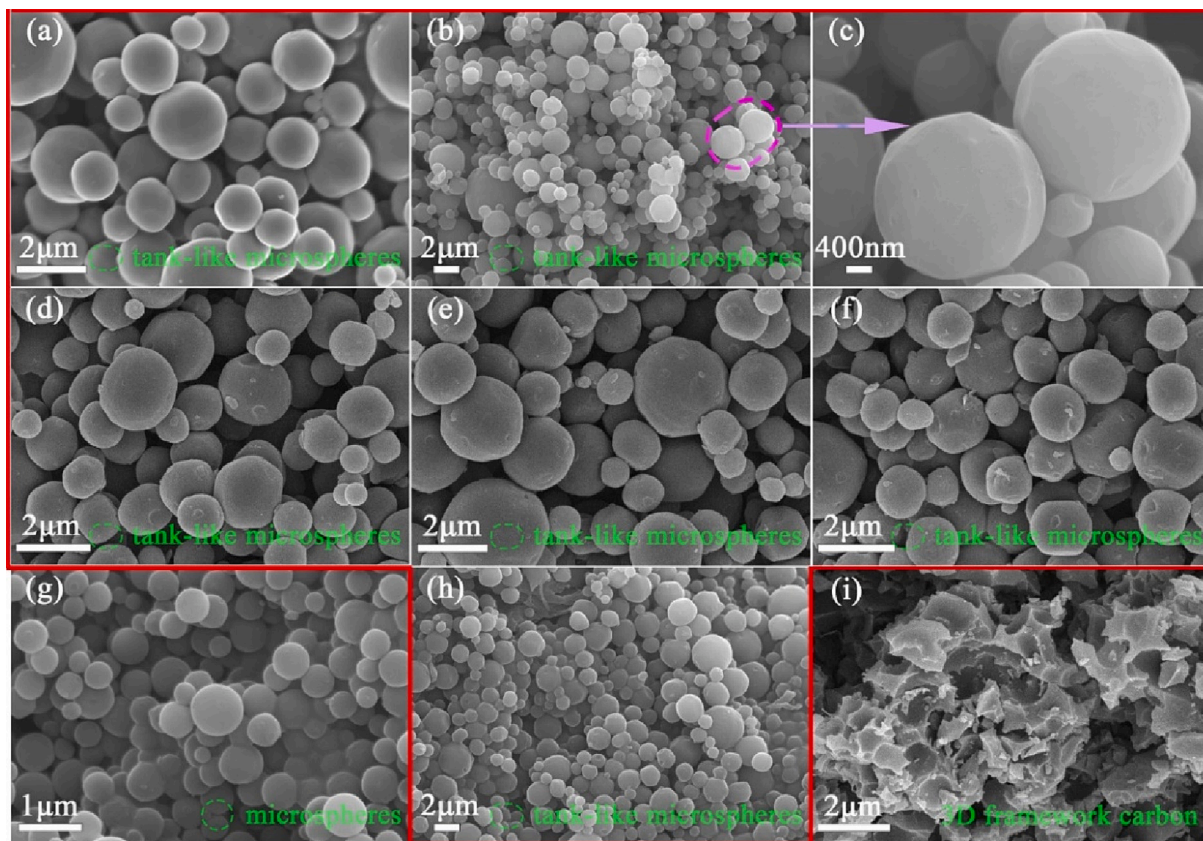


Fig. 2. SEM images of TPCSs (a), TPCSs-2-600 (b, c), TPCSs-1-700 (d), TPCSs-2-600 (e), PCSs-2-600 (f), TPCSs-2-700 (g), TPCSs-2-800 (h), FPC-1-700 (i).

TPCSs-2-700 and TPCSs-2-800 are also prepared at 700 and 800 °C when the mass ratio of KOH to carbon is 2 (Fig. 2e, h). TPCSs-2-Y still show tank-like microspheres morphology and the particle size of TPCSs-2-Y mainly locates at about 1–1.8 μm (Fig. S1c, S1f and S1h), suggesting the activation temperature exerts little influence on their morphology and particle size. For a series of TPCSs-X-700 samples (Fig. 2d–f and Fig. S1e–S1g), they still maintain the shape of tank-like microspheres and the particle size of carbon spheres predominantly distributes in 1–1.8 μm. It is demonstrated that KOH activation has hardly any effect on the morphology and particle size of tank-like microspheres. Therefore, the KOH activator has only corroded along the radial direction to create numerous micropores instead of surface corrosion, which is seen from no change in the morphology and particle size of tank-like microspheres under different activation temperatures and mass of KOH. To our knowledge, the majority of reported resin-based porous carbon possesses sphere-like morphology and has been widely reported in other literature [32,37–39].

Subsequently, other RMF resin-based porous carbon materials have also been prepared by the other two routes. PCSs-2-600 prepared from RMF resin spheres without adding F127 in the synthesis process presents sphere morphology (Fig. 2g), and Fig. S1d exhibits the diameter of the particle is concentrated on the region of 0.35–0.55 μm, which is about one-third that of TPCSs-2-600. It is thus clear that F127 plays a significant role in the preparation of tank-like resin spheres and largely influences the size of resin spheres. On the other hand, FPC-1-700 was prepared by directly heat-treating the mixture of tank-like resin spheres and KOH. It is found that FPC-1-700 is not spheres shape but presents 3D framework carbon structure with the interconnected cavity (Fig. 2i). The structure of FPC-1-700 is tremendously different from that of others and the tank-like microspheres which are destroyed by the activator, which results from resin and KOH forming a molten state in the activation process and generating a large amount of gas during thermal

decomposition process at high temperature.

The microstructures of TPCSs-2-600 were further analyzed by transmission electron microscopy (TEM). TPCSs-2-600 is solid tank-like microsphere with particle diameter of 0.8–1.8 μm and the edge possesses obvious aris (Fig. 3a). Fig. 3b indicates a tank-like microsphere with rotational symmetry (the symmetry axis marked in the image). The height and diameter of tank-like microspheres are about 1.7 μm and 1.9 μm, respectively. It is further proof that TPCSs-2-600 is not a sphere but a tank-like microsphere, which is consistent with SEM results. The HRTEM image of TPCSs-2-600 confirms the existence of abundant amorphous worm-like micropores in the tank-like microspheres due to the activation of KOH [40]. The active interface for storing charge can be furnished by innumerable micropores [41]. Besides, there are a few regular lattice fringes in the TPCSs-2-600 (the red circle marked in the image), which benefits to improve the graphitization degree and conductivity of TPCSs-2-600 (Fig. 3c). The EDS elemental mapping images of TPCSs-2-600 indicate that the C, N, O elements are homogeneously distributed in a tank-like microsphere (Fig. 3d).

The XRD patterns of all samples exhibit similar reflection peaks in Fig. 4a. These reflection peaks located at about 20.8° ~ 21.3° and 42.5° ~ 43.5° correspond to the (002) and (100) plane of carbon material, respectively. Several weak and broad peaks suggest that these carbon materials reveal the character of amorphous carbon and irregular structure, which stemmed from KOH activation. The (002) peak intensity of TPCSs-1-700, TPCSs-2-700, and TPCSs-3-700 gradually decreases as the enhancement of KOH activator [42], suggesting excessive activator leads to overactivation of sample then decreases graphitization degree. The (002) reflection peak intensity for TPCSs-2-700 becomes stronger than that of TPCSs-2-600, demonstrating the crystalline degree of carbon materials increases with the activation temperature (600 °C to 700 °C) [43]. When the activation temperature increases to 800 °C, the peak intensity for TPCSs-2-800 gets weaker than that of TPCSs-2-700.

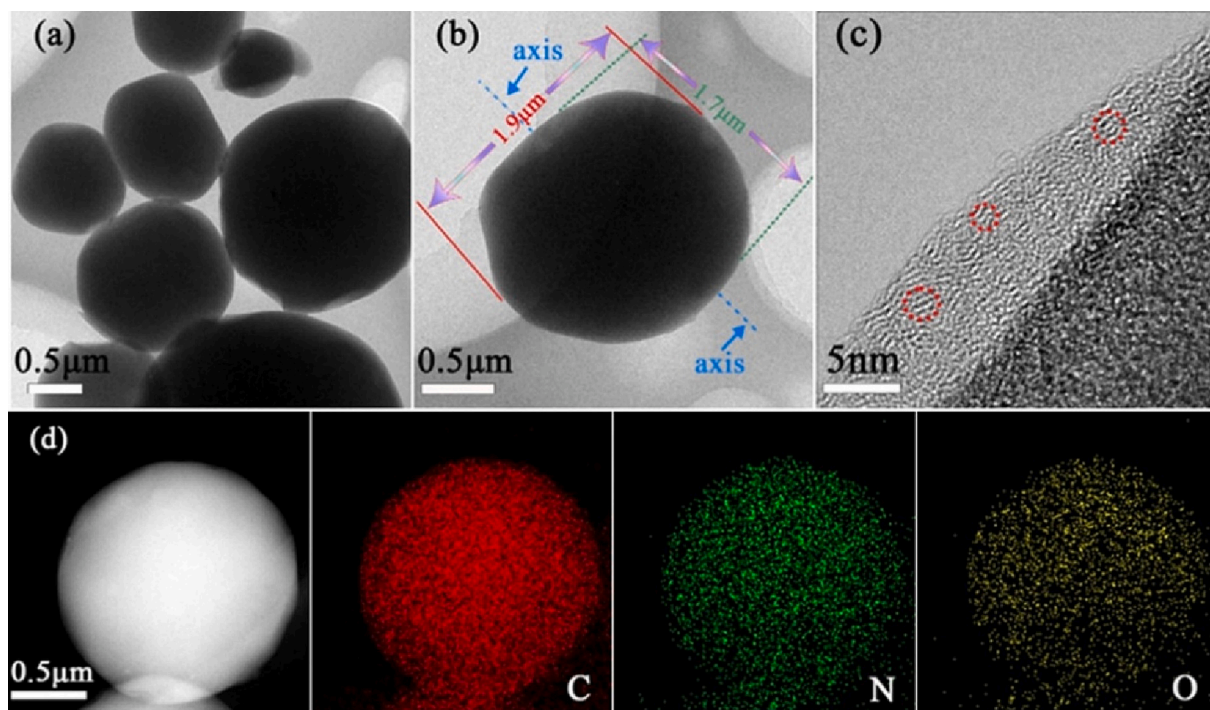


Fig. 3. TEM (a, b), HR-TEM (c) and elemental mapping (d) images of TPCs-2-600.

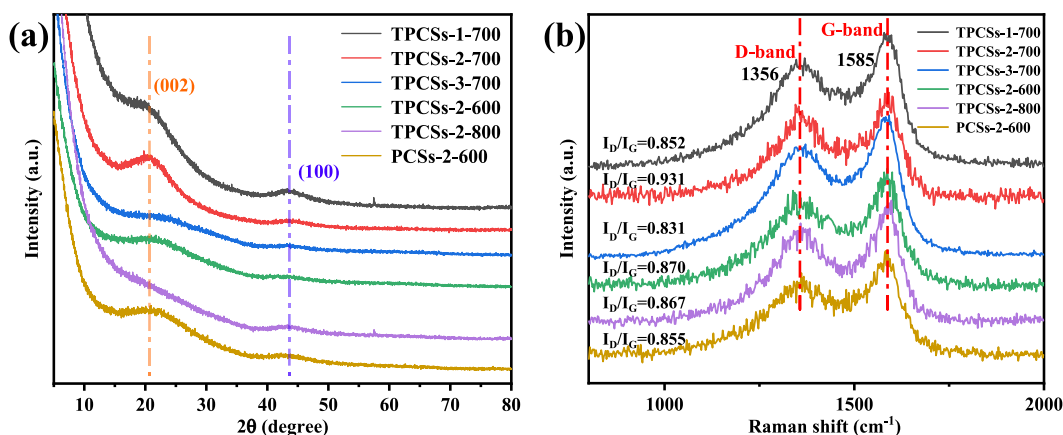


Fig. 4. XRD pattern (a) and Raman spectra (b) of TPCs-1-700, TPCs-2-600, TPCs-2-700, TPCs-2-800, TPCs-3-700. TPCs-1-700, PCSs 2-600.

This result indicates the crystallinity of TPCs-2-800 is lower than that of TPCs-2-700, because the structure of carbon material has been seriously destroyed by KOH and much more amorphous carbon has been created at 800 °C [42]. The peak intensity of PCSs-2-600 is almost the same as that of TPCs-2-600, demonstrating the graphitization degree of PCSs-2-600 cannot be influenced by whether to add the surfactant (F127).

The graphitic nature of all samples is further analyzed by the Raman spectrum (Fig. 4b). All carbon materials possess disorder/defect (D) peaks at 1356 cm^{-1} and graphitic (G) peaks at 1585 cm^{-1} . The intensity ratio of the D band and G band reveals the graphitization or ordered degree of the carbon structure. The values of I_D/I_G for TPCs-1-700, TPCs-2-700, TPCs-3-700, TPCs-2-600, TPCs-2-800, PCSs-2-600 are 0.852, 0.931, 0.831, 0.870, 0.867, 0.855, respectively. The I_D/I_G of all samples is <1 , demonstrating all carbon materials have some crystalline carbon.

To further analyze the surface functional groups and elemental composition of carbon materials, all tank-like microspheres were

studied by XPS technology. Three characteristic peaks are observed at binding energies of 284, 400 and 532 eV (Fig. S2), corresponding to C1s, N1s, and O1s, respectively. Table S1 lists the C, N and O element contents of TPCs-X-Y samples. Wherein, the content of O increases with the activation temperature, which results from the activation degree becomes stronger further to generate a large number of oxygen-containing functional groups that raise the O content of carbon materials surface. The N and O functional groups can increase hydrophilicity for resin-based carbon materials, which benefit that electrolyte easily permeates into carbon materials to further enhance effective specific surface area [43]. The N1s spectrum of these carbon materials can be deconvoluted into three peaks at around 398.75–399.05 eV, 399.55–399.95 eV and 401.2–401.6 eV (Fig. 5a), corresponding to pyridinic-N (N-6), pyrrolic-N (N-5) and quaternary-N (N-Q) [44], respectively. However, the N1s peak of TPCs-3-700 can only be deconvoluted into two peaks corresponding to N-6 and N-5, respectively. Additionally, the proportion of various N and O functional groups are displayed in Fig. 6. For TPCs-2-Y, the content of N-5 decreases gradually, but that of N-6 and N-Q

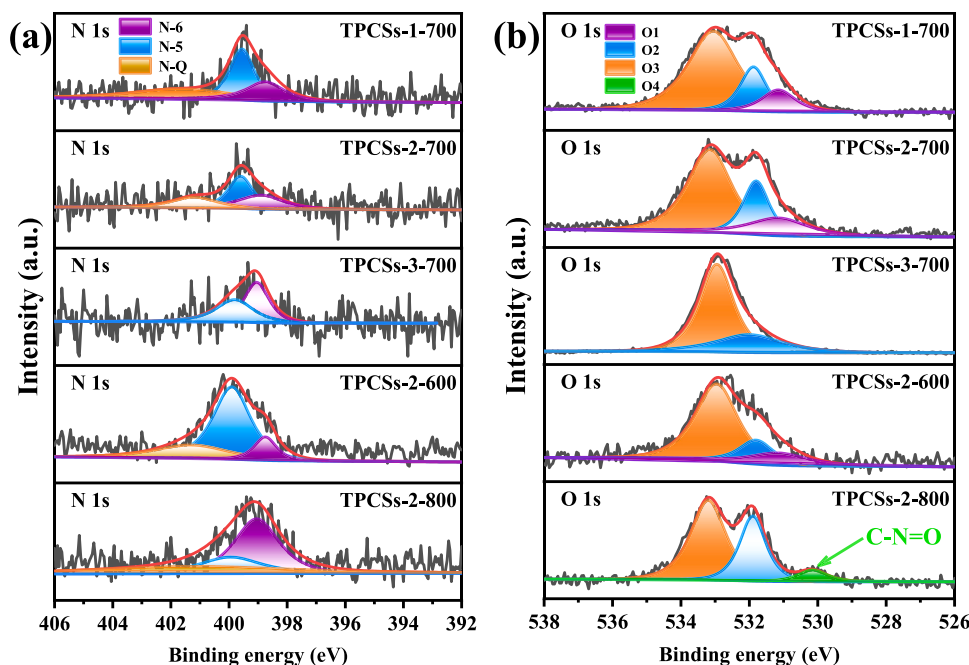


Fig. 5. High resolution N1s XPS spectrum of (a) and O1s XPS spectrum (b) of TPCSSs-1-700, TPCSSs-2-600, TPCSSs-2-700, TPCSSs-2-800 and TPCSSs-3-700.

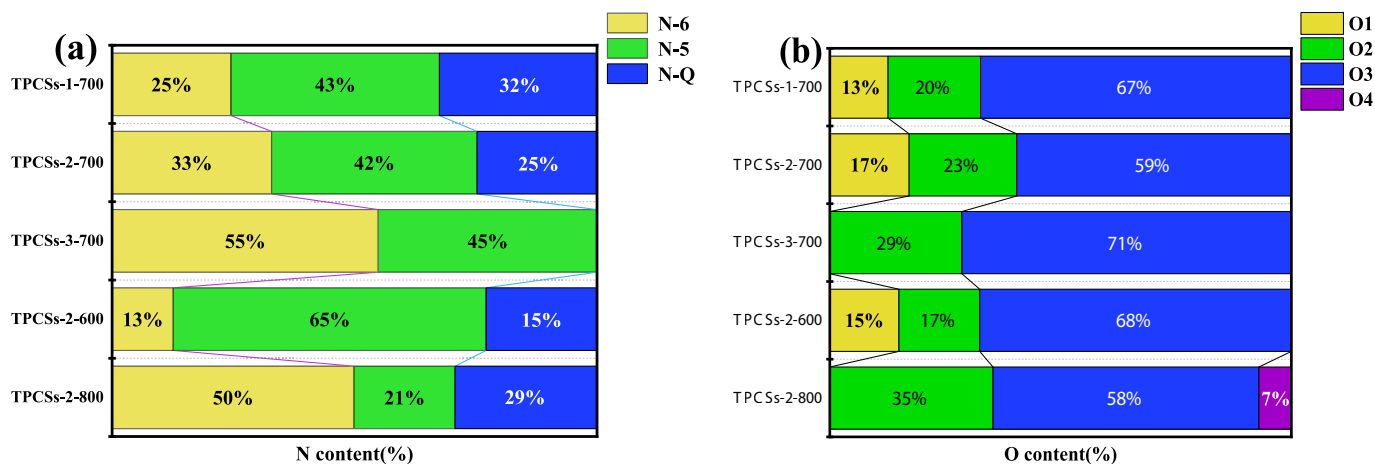


Fig. 6. Various N (a) and O (b) content comparison of the carbon electrodes.

significantly increases with the increase of activation temperature [45,46], suggesting that N-5 has transferred into N-6 and N-Q and possesses poor stability at high temperature. In general, the high temperature speeds up the conversion of N-5 to N-6 and N-Q [47]. The increase of N-6 content is very remarkable when the amount of KOH activator enhances, and the N-Q content evidently decreases with the enhancement of KOH dosages. Obviously, the nitrogen functional group can directly be tuned by activation temperature and the amount of activator. Additionally, N-Q could explicitly enhance the electrical conductivity and charge transfer of carbon materials to boost rate capability and cycling ability for electrodes [40]. N-6 could increase the surface wettability of carbon electrodes, and the N-6 and N-5 species could produce Faraday reactions to increase the capacitance of electrode materials [42].

The O1s XPS curve of these electrodes can be fitted into three peaks at about 531.15, 531.8~532, 532.95~533.2 (Fig. 5b), corresponding to the carbonyl oxygen of quinones (O1), carbon-oxygen double bond (O2) and ether groups and/or phenol groups (O3) [48], respectively. The content of O3 is hardly affected by activation temperature, and the peak

of O3 vanishes followed by the appearance of C-N=O (O4) at 530.15 eV when the activation temperature reaches 800 °C [33]. When the ratio of KOH to TPCSSs reaches 3, the O1s spectra of TPCSSs-3-700 can be only deconvoluted into two peaks situated at 532 and 532.95 eV ascribed to O2 and O3 meanwhile the O1 peak has disappeared, respectively. The content of O2 increases significantly as the increase of the amount of KOH and the activation temperature. It is proved that the content of functional groups could be easily tuned by activation temperature and the amount of KOH activator. Oxygen functional groups of carbon materials play a crucial role in improving the performance of electrochemical and wettability for electrode materials [49].

The specific surface area and pore structure of TPCSSs-1-700, TPCSSs-2-700, TPCSSs-3-700, TPCSSs-2-600 and TPCSSs-2-800 are analyzed by nitrogen adsorption-desorption measurements. As shown in Fig. 7a, the isotherms of all tank-like porous carbon spheres are typical Type I with strong adsorption at $P/P_0 < 0.1$, which represents the existence of abundant micropores in these tank-like microspheres. The curves of pore size distribution reveal the pore sizes of TPCSSs-1-700, TPCSSs-2-700, TPCSSs-3-700, TPCSSs-2-600 and TPCSSs-2-800 predominantly locate at

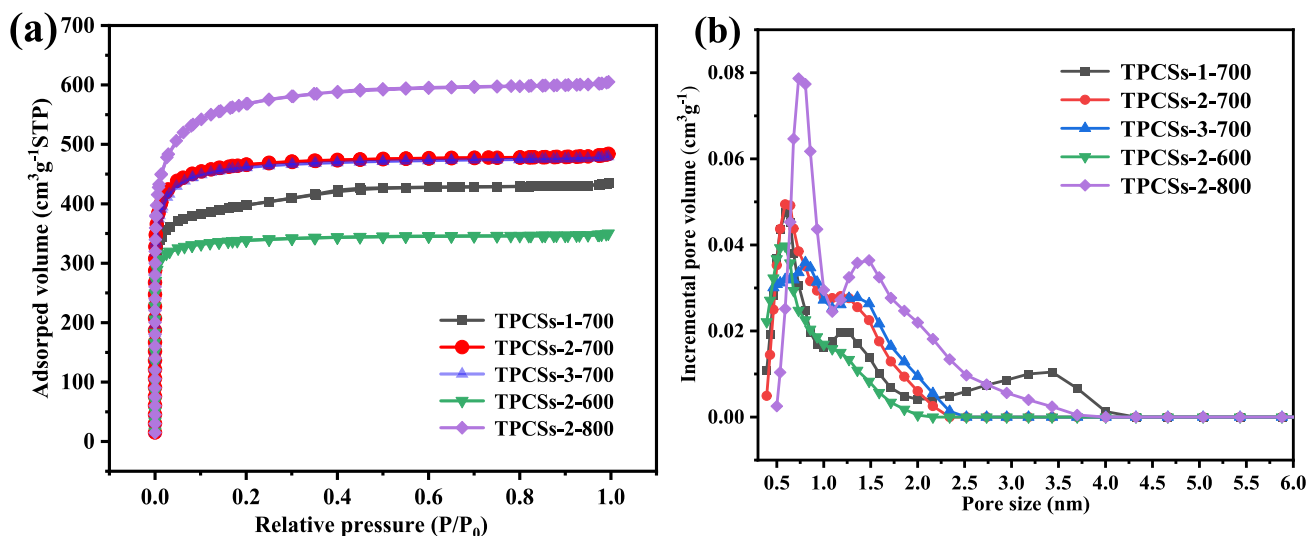


Fig. 7. Nitrogen adsorption-desorption isotherms (a) and pore size distribution (b) of TPCSSs-1-700, TPCSSs-2-700, TPCSSs-3-700, TPCSSs-2-600, TPCSSs-2-800.

0.5–2 nm (Fig. 7b), demonstrating the major existence of micropores in these samples. And there are a few mesopores in the TPCSSs-X-Y with a distribution of 2–4 nm. However, the peaks of TPCSSs-2-600, TPCSSs-2-700 and TPCSSs-2-800 center at 0.536/1.090, 0.590/1.179 and 0.733/1.358 nm, respectively. It is clearly found that pore sizes gradually increase with activation temperature attributed to powerful corrosion between KOH and tank-like carbon microspheres at high temperature.

The specific surface area and pore structure parameters of carbon materials are itemized in Table 1. Among these pore parameters, the specific surface area of TPCSSs-1-700, TPCSSs-2-700, TPCSSs-3-700, TPCSSs-2-600, and TPCSSs-2-800 are 1515, 1797, 1779, 1338 and 2149 m² g⁻¹, respectively. And the microporous specific surface area accounts for >91 % of the total specific surface area. When the activation temperature is 700 °C, the specific surface area obviously enhances as increasing the mass ratio of KOH to carbon from 1 to 2 and does not change when the mass ratio of KOH to carbon enhances from 2 to 3. The pore volume and specific surface area increase with activation temperature when the mass ratio of KOH to carbon is 2, suggesting the etching degree of carbon by KOH increases with activation temperature. In summary, the as-prepared tank-like carbon spheres mainly possess micropores.

3.2. Electrochemical performances

The electrochemical performance of resin-based carbon materials was investigated in 6 M KOH electrolyte in a three-electrode system. As

Table 1

Pore structure parameters of the TPCSSs-1-700, TPCSSs-2-600, TPCSSs-2-700, TPCSSs-2-800, TPCSSs-3-700.

Sample	S_{BET}^a (m ² g ⁻¹)	S_{mic}^b (m ² g ⁻¹)	V_{total}^c (cm ³ g ⁻¹)	V_{micro}^b (m ³ g ⁻¹)	D_{aver}^d (nm)
TPCSSs-1-700	1515	1482	0.67	0.64	2.70
TPCSSs-2-700	1797	1749	0.75	0.70	2.77
TPCSSs-3-700	1779	1700	0.74	0.68	2.71
TPCSSs-2-600	1338	1289	0.54	0.50	2.79
TPCSSs-2-800	2149	1954	0.94	0.80	2.57

^a Total surface area calculated by the BET method.

^b Micropore surface area and volume calculated from t-plot method.

^c Total pore volume calculated at $P/P_0 = 0.99$.

^d Average pore diameter calculated from BJH desorption.

shown in Fig. 8a, the cyclic voltammetry (CV) curves of these carbon electrodes present a rectangular-like shape at a scan rate of 10 mV s⁻¹ with a well-defined spacious peak at a potential window from -0.8 to -0.1 V, suggesting the specific capacitance is composed of electrical double-layer capacitor (EDLC) and pseudocapacitance [41,50]. Wherein, the TPCSSs-2-600 and PCSs-2-600 carbon electrodes possess the most evident hump, demonstrating plenty of pseudocapacitance reactions happens in which. The redox hump of the CV curve could be caused by the reversible faradaic reaction from plentiful nitrogen and oxygen-containing functional groups on the surface of carbon electrodes [51]. However, the humps of CV curves for TPCSSs-2-Y gradually become smaller with the enhancement of activation temperature from 600 °C to 800 °C and even disappears at 800 °C, indicating that the pseudocapacitance reactions became infrequent for the porous carbon obtained at higher activation temperature. This result is attributable to the content of nitrogen heteroatoms decreasing with the increase of activation temperature. Besides, the rectangular area of the CV curve for TPCSSs-2-600 possesses the largest closed area in all carbon electrodes, demonstrating the specific gravimetric capacitance for TPCSSs-2-600 is higher than that of others [52]. The CV curve at a scan rate of 50 mV s⁻¹ remains rectangle-like with a slight twist in shape, demonstrating the TPCSSs-2-600 electrode has a relatively low rate capability derived from poor charge transfer and ion transfer in high scan rate (Fig. S3a) [53]. This results from the low electrical conductivity, massive pseudocapacitance reactions and smaller pore size (mainly centered at <2 nm seen from Fig. 7b) for TPCSSs-2-600 electrode.

The galvanostatic charge/discharge (GCD) curves show a slightly distorted geometric triangle at the current density of 1 A g⁻¹ (Fig. 8b), which represents the immaculate coulombic efficiency and further proves the existence of extra pseudo-capacitance [40,43]. Specifically, the calculated specific capacitances of TPCSSs, TPCSSs-1-700, TPCSSs-2-700, TPCSSs-3-700, TPCSSs-2-600, TPCSSs-2-800, PCSs-2-600 are 14.9, 284, 303, 273, 328, 221 and 314 F g⁻¹ (Fig. 8c), respectively. Obviously, the specific capacitance of resin-based carbon electrodes distinctly improves via KOH activation, which is seen from the specific capacitance of TPCSSs-1-700 is far higher than that of TPCSSs. The TPCSSs-2-700 (303 F g⁻¹) has a higher capacitance than that of TPCSSs-1-700 (284 F g⁻¹) and TPCSSs-3-700 (273 F g⁻¹). The specific gravimetric capacitance for the porous carbon prepared at various KOH dosages increases first and then decreases with raising the KOH dosage, which is agree with the change trend of surface area (Table 1). Moreover, the specific capacitance for TPCSSs-2-Y electrodes gradually reduces with the raise of activation temperature from 600 °C to 800 °C, which is contrary to the change trend of surface area. This result illustrates that the effective

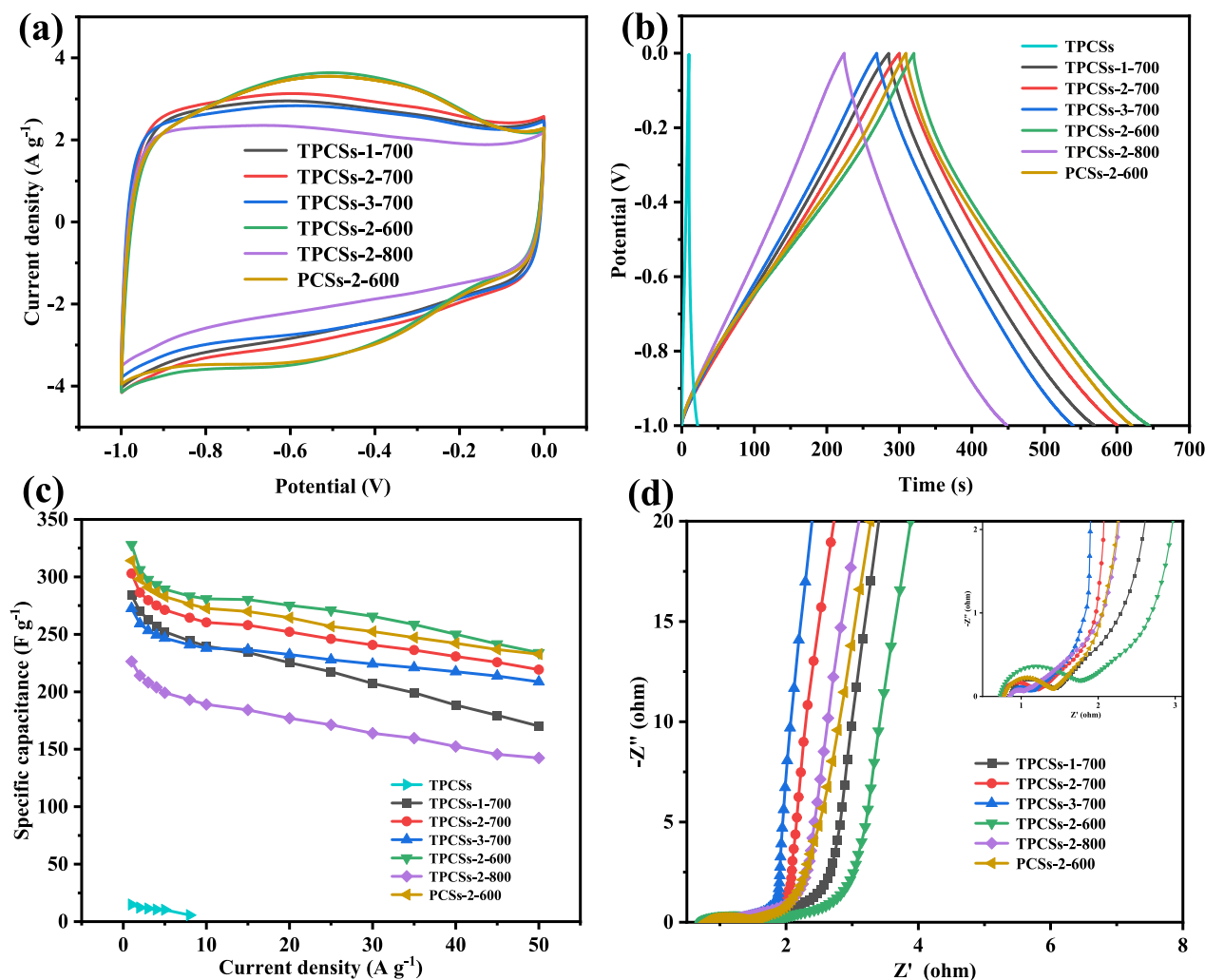


Fig. 8. Electrochemical performance of all resin-based carbon materials measured in a three-electrode system in the 6 M KOH electrolyte: (a) CV curves at 10 mV s^{-1} ; (b) GCD curves at a current density of 1 A g^{-1} ; (c) specific capacitances calculated at different current densities; (d) Nyquist plot.

electrochemical interfacial area is lower for the carbon electrode obtained at high activation temperature. In addition, the decrease of specific capacitance with raising the activation temperature has relation with the less of pseudocapacitance reaction and the increase of pore size (seen from Fig. 7b) as well. The GCD curves shape of TPCSS-2-600 hardly any change when different current density increases from 1 to 20 A g^{-1} (Fig. S3b).

The specific capacitance of all the resin-derived carbon materials at various current densities are displayed in the Fig. 8c. The specific gravimetric capacitance of TPCSS-2-600 is higher than that of others at all current densities, stemming from the highest N content and suitable pore size. The addition of F127 in the synthesis process of resin spheres has little influence on the specific capacitance of resin-derived carbon materials (TPCSS-2-600 and PCSs-2-600). The specific capacitance of TPCSS-2-600 even maintains at 234 F g^{-1} at the high current density of 50 A g^{-1} , and the capacitance retention is 71.3 %. Furthermore, the electrochemical performance of TPCSS-2-600 have been made compared with other previously reported resin-based carbon materials (Table 2). It is found the electrochemical performance of TPCSS-2-600 possesses certain superiority over other resin-based carbon materials. The corresponding specific capacitance of TPCSS-1-700, TPCSS-2-700, TPCSS-3-700, TPCSS-2-800 and PCSs-2-600 carbon electrodes are 170, 219, 209, 142 and 233 with the capacitance retention rate of 59.8 %, 72.3 %, 76.5 %, 62.9 % and 74.1 % when the current density reaches 50 A g^{-1} , respectively. The capacitance retention rate remarkably enhances from

Table 2

Comparison of electrochemical performances of recently reported resin-based porous carbon.

Sample	Electrolyte	Specific capacitance (F g^{-1})	Capacitance retention	Ref.
N-MCS	6 M KOH	278 (1 A g^{-1})	78 % (10 A g^{-1})	[8]
HPCSs	6 M KOH	321 (0.5 A g^{-1})	72.9 % (50 A g^{-1})	[32]
CS-R	6 M KOH	235 (1 A g^{-1})	73.2 % (10 A g^{-1})	[37]
N/B-OMC	6 M KOH	272 (0.5 A g^{-1})	80.8 % (10 A g^{-1})	[54]
TPCSS-2-600	6 M KOH	328 (1 A g^{-1})	71.3 % (50 A g^{-1})	This work

59.8 % to 76.5 % with the mass of KOH, which results from the pore size becoming larger (Fig. 7b) further improving the transport of electrolyte ions. and the larger pore size is profit to electrolyte ions transfer in resin-based carbon materials.

To explore the charge transfer ability and ion transfer of all carbon electrodes, the electrochemical impedance spectroscopy (EIS) measurement was carried out (Fig. 8d). The Nyquist plots of all carbon electrode exhibit alike curves, which consist of a line practically perpendicular to the real part in the low-frequency region, an inclined line (about 45°) in the middle-frequency region attributed to the Warburg impedance and a semicircle at the high frequency [55,56]. The curve intercept in the high-frequency region of the real axis is equivalent series resistance (R_s) [57], which composes of the basic resistance of the

activated electrode, the resistance of electrolyte solution and the contact resistance between the interfaces of electrodes, electrolyte and the current collector. The R_s value are 0.85, 0.73, 0.86, 0.73, 0.83, 0.78 Ω for TPCSSs-1-700, TPCSSs-2-700, TPCSSs-3-700, TPCSSs-2-600, TPCSSs-2-800, PCSs-2-600, respectively. TPCSSs-2-600 and PCSs-2-600 possess lower R_s values (0.73 Ω) than that of other electrodes. The charge transfer resistance (R_{ct}) is determined by the diameter of the semicircle [54], interrelated with the pore structure (Table 1) and the containing N or O functional groups. The R_{ct} value of TPCSSs-1-700, TPCSSs-2-700, TPCSSs-3-700, TPCSSs-2-600, TPCSSs-2-800, PCSs-2-600 is 0.59, 0.49, 0.25, 1.04, 0.30, 0.62 Ω , respectively. The electrode of TPCSSs-2-600 possesses the highest R_{ct} value in all carbon electrodes, which could be attributed to the abundant Faradaic reactions produced by the high content of N functional groups. And the R_{ct} value of TPCSSs-2-600 electrode is higher than that of others, which results from its relatively poor pore structure and low specific surface area (Table 1). Furthermore, the constant of relaxation time (the formula: $\tau_o = 1/f$, f represents frequency at -45°) acquired from the Bode curve (Fig.S3c). The constant of relaxation time of TPCSSs-1-700, TPCSSs-2-700, TPCSSs-3-700, TPCSSs-2-600, TPCSSs-2-800, PCSs-2-600 are 6.06, 5.56, 4.55, 7.41, 3.23 5.26, respectively. The relaxation time constant reduces along the enhancement of activation temperature and activator mass. The carbon electrode with the low value of relaxation time constant has rapid electrolyte ions diffusion ability. Thus, TPCSSs-2-600 possesses a relatively poor ions transport and diffusion ability seen from its higher relaxation time constant.

To explore the proportion of pseudocapacitance in total specific capacitance caused by nitrogen and oxygen functional groups, the discharge curves can be divided into two parts resulting from curves with different slopes when the potential of the work electrode is lower than -0.1 V. The linear part at high potential indicates electric double-layer capacitance (EDLC) and another part (curve region) with slight deformation at low potential presents the integration of EDLC and pseudocapacitance (Fig. 9) [58]. The line part lengthens and intersects with lateral axis, and the intercept represents the discharge time (T_D) of the EDLC. T_p is the pseudocapacitance time which is obtained from the

total discharge time minus T_D . The corresponding pseudocapacitance calculated from T_p of the TPCSSs-2-600, TPCSSs-2-700, TPCSSs-2-800, TPCSSs-1-700 and TPCSSs-3-700 carbon electrodes is 218, 174, 110, 152 and 136 $F g^{-1}$ at the low current density of $1 A g^{-1}$ with the proportion of 67.1 %, 58 %, 48.8 %, 53.5 % and 52.9 % for the overall specific capacitance, respectively. The TPCSSs-2-600 has the highest pseudocapacitance proportion, which can be confirmed by the most obvious pseudocapacitance peak in the CV curve (Fig. 8a). To further investigate the electrochemical performance of these carbon electrodes, the symmetrical device was fabricated by two identical electrodes in 6 M KOH aqueous electrolyte. The CV (Fig. 10a) and GCD (Fig. 10b) curves of all samples present quasi-rectangular and isosceles triangles with slight deformation. It is indicated that their specific capacitance consists of EDLC and pseudocapacitance. The humps of CV curves for carbon electrodes gradually get smaller when activation temperature enhances from $600^\circ C$ to $800^\circ C$ and that for TPCSSs-2-800 almost vanishes, suggesting that more pseudocapacitance reactions happen in the porous carbon spheres obtained at low activation temperature because of more nitrogen-containing functional groups existed in carbon spheres. The specific capacitance of TPCSSs at $1 A g^{-1}$ is low as $14.9 F g^{-1}$ in the three-electrode system, but the calculated capacitance of TPCSSs nearly is very small in a symmetrical system at the current density of $1 A g^{-1}$. Thus, the electrochemical data of TPCSSs is not embodied in two-electrode system. In Fig. 10c, the specific capacitances of TPCSSs-1-700, TPCSSs-2-700, TPCSSs-3-700, TPCSSs-2-600, TPCSSs-2-800 and PCSs-2-600 electrodes are 191, 205, 190, 210, 157, 216 $F g^{-1}$ at $1 A g^{-1}$, respectively. TPCSSs-1-700, TPCSSs-2-700, TPCSSs-3-700 possess the specific capacitance of 111, 136 and $141.4 F g^{-1}$ at $15 A g^{-1}$ with corresponding retention of 58 %, 66.2 % and 74.4 %. With increasing KOH activator, the specific capacitance of resin-based carbon materials initially rises and later falls at low current density, but that gradually increases at higher current density, and the rate capability of resin-based carbon spheres gradually boosts due to pore size getting much larger further to facilitate electrolyte ions transport, which is consistent with three-electrode system results. The specific capacitance of TPCSSs-2-600, TPCSSs-2-800 and PCSs-2-600 are 75.3, 104 and $129.8 F g^{-1}$ with the capacitance retention rate

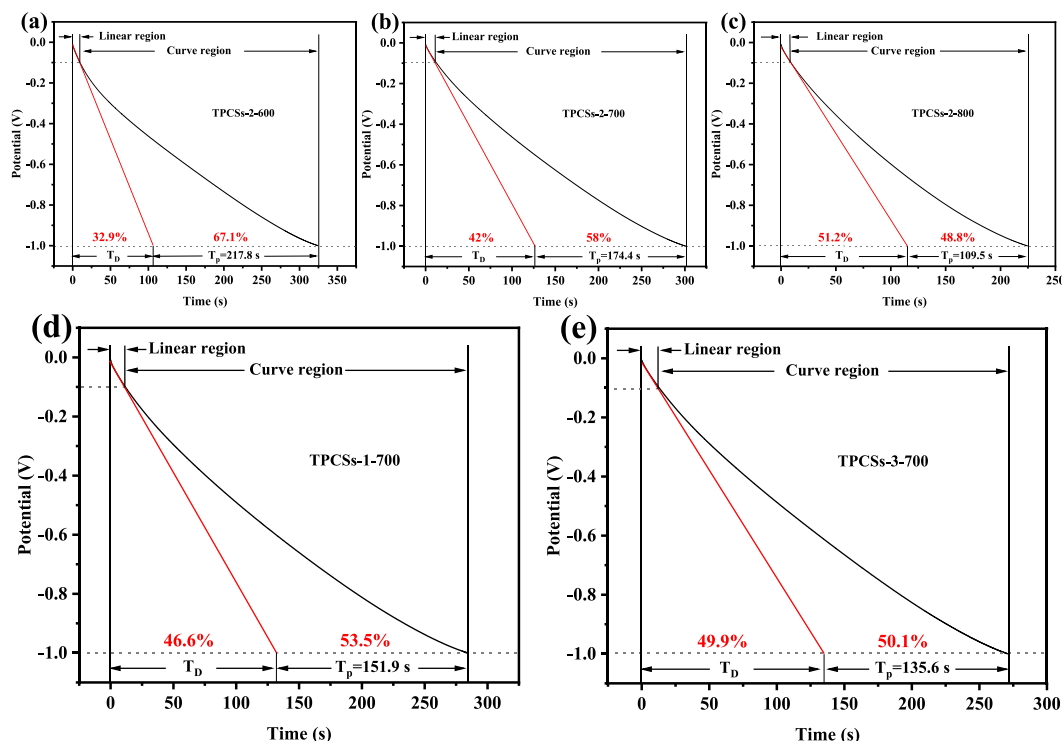


Fig. 9. Discharge time of the pseudocapacitance parts of (a) TPCSSs-2-600, (b) TPCSSs-2-700, (c) TPCSSs-2-800, (d) TPCSSs-1-700 and (e) TPCSSs-3-700.

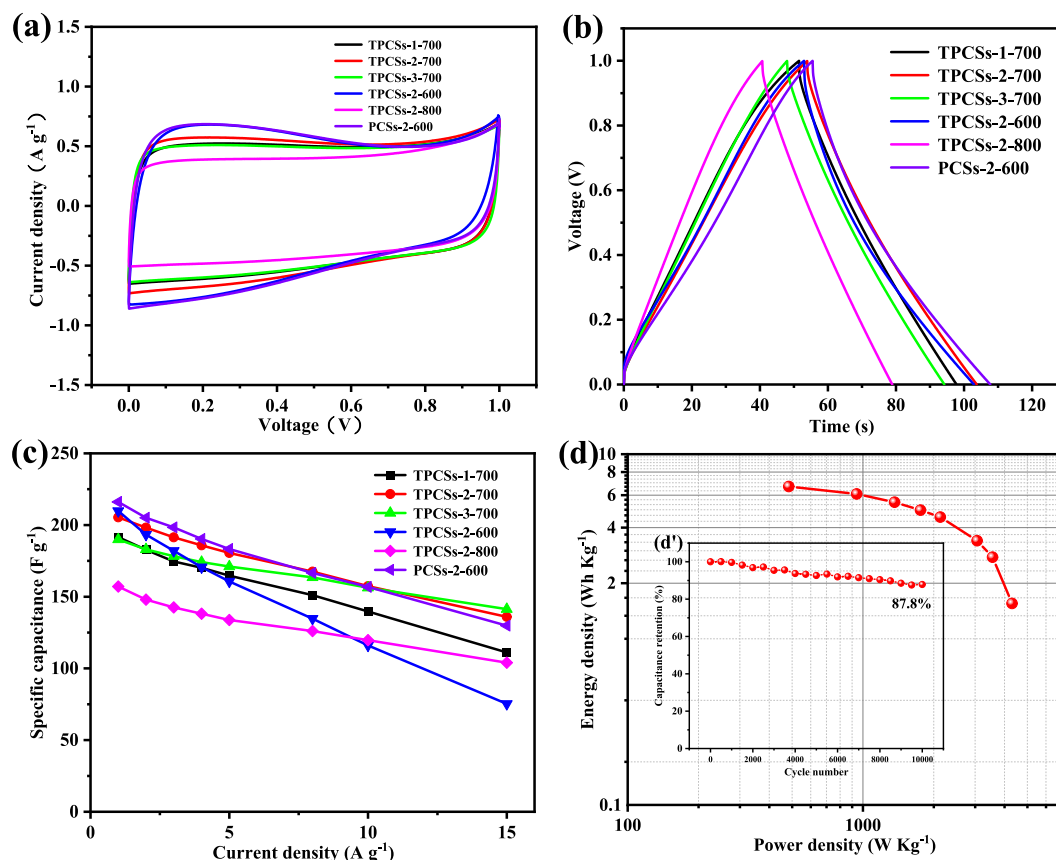


Fig. 10. Electrochemical performances of TPCSS-X-Y and PCSs-2-600 in the symmetrical system in the 6 M KOH electrolyte: (a) CV curves of 10 mV s⁻¹; (b) GCD curves of 1 A g⁻¹; (c) the specific capacitance at different current densities; (d) Ragone plot of TPCSS-2-700 device in the symmetrical system; (d') cycle stability of TPCSS-2-600 at the current density of 10 A g⁻¹ in 6 M KOH.

of 35.9 %, 66.3 % and 60.1 % at the high current density of 15 A g⁻¹, respectively. The specific capacitance at 1 A g⁻¹ for resin-based porous carbon decreases as the increase of activation temperature, which results from effective electrochemical interface getting lower at high activation temperature. The rate performance of carbon electrode enhances when activation temperature increases from 600 °C to 800 °C due to broad pore structure further elevating electrolyte ions diffusion ability. The energy density and power density of the TPCSS-2-700 symmetric supercapacitor are shown in the Ragone plots (Fig. 10d) and the electrode exhibits a good energy density of 6.68 Wh kg⁻¹ with a power density of 484 W kg⁻¹. The capacitance retention of TPCSS-2-600 electrode reaches up to 87.8 % after 10,000 cycle numbers at the high current density of 10 A g⁻¹ in two-electrode system (Fig. 10d'), suggesting the symmetrical supercapacitor has an outstanding cycling stability.

4. Conclusions

In summary, the tank-like resorcinol-melamine-formaldehyde (RMF) resin spheres are firstly prepared via the hydrothermal method with the assistance of F127, and RMF resin spheres are obtained without adding F127 in the synthesis process. The F127 plays a crucial role in directly tuning the morphology and particle size of RMF resin. The ultimate tank-like resin-based porous carbon spheres are produced by the pre-carbonization of RMF resin and then KOH activation. The KOH dosage and activation temperature exert hardly any influences on the morphology and size of the final tank-like resin-based porous carbon. There are almost no mesopores in the tank-like porous carbon spheres with KOH activation, and the specific capacitance of tank-like resin-based carbon electrodes distinctly enhances after KOH activation. The specific surface

area for resin-based carbon materials increases first and then decreases with increasing KOH activator, and further affects the specific capacitance with the same change trend of surface area variation of resin-based porous carbon. Meanwhile, the resin-based porous carbon materials show more outstanding rate performance along increasing the KOH dosage, which results from the pore size getting larger further to enhance ions transport ability. As the activation temperature increases, the specific surface area of the resin-based porous carbon sphere becomes higher, but the efficient electrochemical interface and pseudo-capacitive reaction get lower, and the pore size becomes larger, which reduces the specific capacitance of the carbon electrode. The symmetrical supercapacitor of TPCSS-2-600 has excellent cycle stability with 87.8 % after 10,000 cycle numbers at 10 A g⁻¹, and TPCSS-2-700 shows a good energy density of 6.68 Wh kg⁻¹ with a power density of 483.98 W kg⁻¹ in 6 M KOH aqueous electrolyte.

CRediT authorship contribution statement

Xin Cui was responsible for experiment, analysis and writing. Yuchen Jiang and Zhifeng He were responsible for drawing some figures. Zeyi Liu and Xiaoyang Yang were responsible for setting some experimental testing. Jiafeng Wan and Yifu Liu participated in data analysis. Fangwei Ma was responsible for reviewing & editing the manuscript.

Declaration of competing interest

The authors declare that they have no known competing financial interests or personal relationships that could have appeared to influence the work reported in this paper.

Data availability

The authors do not have permission to share data.

Acknowledgements

The authors would like to acknowledge the funding from from Natural Science Foundation of Heilongjiang Province of China (LH2022B018) and the Youth Science and Technology Innovation Team Project of Heilongjiang Province (2021-KYYWF-0030)

Appendix A. Supplementary data

Supplementary data to this article can be found online at <https://doi.org/10.1016/j.diamond.2023.110054>.

References

- [1] M. Zhong, M. Zhang, X. Li, Carbon nanomaterials and their composites for supercapacitors, *Carbon*, **4** (2022) 950–985.
- [2] P. Simon, Y. Gogotsi, Perspectives for electrochemical capacitors and related devices, *Nat. Mater.* **19** (2020) 1151–1163.
- [3] S. Zheng, H. Xue, H. Pang, Supercapacitors based on metal coordination materials, *Coord. Chem. Rev.* **373** (2018) 2–21.
- [4] A. Noori, M.F. El-Kady, M.S. Rahmanifar, R.B. Kaner, M.F. Mousavi, Towards establishing standard performance metrics for batteries, supercapacitors and beyond, *Chem. Soc. Rev.* **48** (2019) 1272–1341.
- [5] Y. Fang, Q. Zhang, L. Cui, Recent progress of mesoporous materials for high performance supercapacitors, *Microporous Mesoporous Mater.* **314** (2021), 110870.
- [6] F. Wang, X. Wu, X. Yuan, Z. Liu, Y. Zhang, L. Fu, Y. Zhu, Q. Zhou, Y. Wu, W. Huang, Latest advances in supercapacitors: from new electrode materials to novel device designs, *Chem. Soc. Rev.* **46** (2017) 6816–6854.
- [7] D.P. Dubal, N.R. Chodankar, D.-H. Kim, P. Gomez-Romero, Towards flexible solid-state supercapacitors for smart and wearable electronics, *Chem. Soc. Rev.* **47** (2018) 2065–2129.
- [8] Y. Mo, J. Du, H. Lv, Y. Zhang, A. Chen, N-doped mesoporous carbon nanosheets for supercapacitors with high performance, *Diam. Relat. Mater.* **111** (2021), 108206.
- [9] T. Liu, G. Liu, Block copolymer-based porous carbons for supercapacitors, *J. Mater. Chem. A* **7** (2019) 23476–23488.
- [10] E.S. Goda, S. Lee, M. Sohail, K.R. Yoon, Prussian blue and its analogues as advanced supercapacitor electrodes, *Journal of Energy Chemistry*, **50** (2020) 206–229.
- [11] Z. Li, J. Lin, B. Li, C. Yu, H. Wang, Q. Li, Construction of heteroatom-doped and three-dimensional graphene materials for the applications in supercapacitors: a review, *Journal of Energy Storage*, **44** (2021), 103437.
- [12] Y.-Z. Zhang, Y. Wang, T. Cheng, L.-Q. Yao, X. Li, W.-Y. Lai, W. Huang, Printed supercapacitors: materials, printing and applications, *Chem. Soc. Rev.* **48** (2019) 3229–3264.
- [13] X. Zhang, X. Meng, Q. Wang, B. Qin, L. Jin, Q. Cao, Preparation and electrochemical investigation of polyaniline nanowires for high performance supercapacitor, *Mater. Lett.* **217** (2018) 312–315.
- [14] Y. Wang, Y. Song, Y. Xia, Electrochemical capacitors: mechanism, materials, systems, characterization and applications, *Chem. Soc. Rev.* **45** (2016) 5925–5950.
- [15] X. Gang, M. Krishnamoorthy, W. Jiang, J. Pan, Z. Pan, X. Liu, A novel in-situ preparation of N-rich spherical porous carbon as greatly enhanced material for high-performance supercapacitors, *Carbon*, **171** (2021) 62–71.
- [16] S. Sun, L. Wang, H. Xu, Characteristics of graphite oxide membranes with different thickness by low temperature thermal reduction for aqueous EDLC electrodes and hot activation phenomenon, *Mater. Res. Bull.* **154** (2022), 111927.
- [17] L. Peng, H. Peng, C.-T. Hung, D. Guo, L. Duan, B. Ma, L. Liu, W. Li, D. Zhao, Programmable synthesis of radially gradient-structured mesoporous carbon nanospheres with tunable core-shell architectures, *Chem.* **7** (2021) 1020–1032.
- [18] W. Tian, H. Zhang, X. Duan, H. Sun, G. Shao, S. Wang, Porous carbons: structure-oriented design and versatile applications, *Adv. Funct. Mater.* **30** (2020) 1909265.
- [19] H. Wang, Y. Shao, S. Mei, Y. Lu, M. Zhang, J. Sun, K. Matyjaszewski, M. Antonietti, J. Yuan, Polymer-derived heteroatom-doped porous carbon materials, *Chem. Rev.* **120** (2020) 9363–9419.
- [20] X. Zhang, K. Zhang, H. Li, Q. Cao, L. Jin, P. Li, Porous graphitic carbon microtubes derived from willow catkins as a substrate of MnO₂ for supercapacitors, *J. Power Sources* **344** (2017) 176–184.
- [21] X. Luo, Y. Chen, Y. Mo, A review of charge storage in porous carbon-based supercapacitors, *New Carbon Materials*, **36** (2021) 49–68.
- [22] F. Ma, L. Sun, H. Zhao, Q. Li, L. Huo, T. Xia, S. Gao, Supercapacitor performance of hollow carbon spheres by direct pyrolysis of melamine-formaldehyde resin spheres, *Chem. Res. Chin. Univ.* **29** (2013) 735–742.
- [23] J. Du, A. Chen, X. Gao, Y. Zhang, H. Lv, Reasonable construction of hollow carbon spheres with an adjustable shell surface for supercapacitors, *ACS Appl. Mater. Interfaces* **14** (2022) 11750–11757.
- [24] L. Peng, C.-T. Hung, S. Wang, X. Zhang, X. Zhu, Z. Zhao, C. Wang, Y. Tang, W. Li, D. Zhao, Versatile Nanoemulsion assembly approach to synthesize functional mesoporous carbon Nanospheres with tunable pore sizes and architectures, *J. Am. Chem. Soc.* **141** (2019) 7073–7080.
- [25] B. Liu, L. Wang, Y. Zhang, J. Du, A. Chen, Monomer self-deposition synthesis of N-doped mesoporous carbon tubes using halloysite as template for supercapacitors, *J. Mater. Sci.* **56** (2021) 3312–3324.
- [26] J. Du, Y. Zhang, H. Lv, A. Chen, Silicate-assisted activation of biomass towards N-doped porous carbon sheets for supercapacitors, *J. Alloys Compd.* **853** (2021), 157091.
- [27] D.-W. Kim, H.-S. Kil, K. Nakabayashi, S.-H. Yoon, J. Miyawaki, Structural elucidation of physical and chemical activation mechanisms based on the microdomain structure model, *Carbon*, **114** (2017) 98–105.
- [28] J. Liu, N.P. Wickramaratne, S.Z. Qiao, M. Jaroniec, Molecular-based design and emerging applications of nanoporous carbon spheres, *Nature Mater.* **14** (2015) 763–774.
- [29] T. Yang, R. Zhou, D.-W. Wang, S.P. Jiang, Y. Yamauchi, S.Z. Qiao, M.J. Monteiro, J. Liu, Hierarchical mesoporous yolk-shell structured carbonaceous nanospheres for high performance electrochemical capacitive energy storage, *Chem. Commun.* **51** (2015) 2518–2521.
- [30] J. Liu, S.Z. Qiao, H. Liu, J. Chen, A. Orpe, D. Zhao, G.Q.M. Lu, Extension of the Stöber method to the preparation of monodisperse resorcinol-formaldehyde resin polymer and carbon spheres, *Angew. Chem.* **123** (2011) 6069–6073.
- [31] F. Ma, H. Zhao, L. Sun, Q. Li, L. Huo, T. Xia, S. Gao, G. Pang, Z. Shi, S. Feng, A facile route for nitrogen-doped hollow graphitic carbon spheres with superior performance in supercapacitors, *J. Mater. Chem.* **22** (2012) 13464.
- [32] Z. Liang, H. Xia, L. Zhang, H. Liu, Y. Zhao, H. Li, W. Xie, One-pot synthesis of monodisperse phenolic resin spheres with high thermal stability and its derived carbon spheres as supercapacitor electrodes, *Results in Physics*, **16** (2020), 102912.
- [33] Y. Zhu, Y. Liu, Z. Ge, Y. Zhang, M. Li, S. Wei, Improved thermal stability of melamine resin spheres and electrochemical properties of their carbon derivatives induced by F127, *J. Mater. Sci.* **55** (2020) 12114–12126.
- [34] Y. Jiang, Y. Du, Z. He, F. Ma, Preparation of mesoporous carbon nanospheres from resorcinol/melamine resins and performances of supercapacitors, *Journal of Engineering of Heilongjiang University*, **12** (2021) 31–36.
- [35] M. Wang, H. Liu, D.D. Zhai, X.Y. Chen, Z.J. Zhang, In-situ synthesis of highly nitrogen, sulfur co-doped carbon nanosheets from melamine-formaldehyde-thiourea resin with improved cycling stability and energy density for supercapacitors, *J. Power Sources* **416** (2019) 79–88.
- [36] A. Chen, Y. Yu, Y. Zhang, W. Zang, Y. Yu, Y. Zhang, S. Shen, J. Zhang, Aqueous-phase synthesis of nitrogen-doped ordered mesoporous carbon nanospheres as an efficient adsorbent for acidic gases, *Carbon*, **80** (2014) 19–27.
- [37] H. Yao, J. Zhang, J. Du, B. Li, S. Zong, A. Chen, Carbon spheres prepared by amino acid-catalyzed resorcinol-formaldehyde polymerization for supercapacitors, *J. Alloys Compd.* **926** (2022), 166948.
- [38] F. Wang, Y. Wang, Y. Fang, J. Zhu, X. Li, J. Qi, W. Wu, Synthesis of nitrogen-doped flower-like carbon microspheres from urea-formaldehyde resins for high-performance supercapacitor, *J. Alloys Compd.* **812** (2020), 152109.
- [39] J. Du, L. Liu, Y. Yu, H. Lv, Y. Zhang, A. Chen, Confined pyrolysis for direct conversion of solid resin spheres into yolk-shell carbon spheres for supercapacitor, *J. Mater. Chem. A* **7** (2019) 1038–1044.
- [40] Y. Jiang, Z. He, Y. Du, J. Wan, Y. Liu, F. Ma, In-situ ZnO template preparation of coal tar pitch-based porous carbon-sheet microsphere for supercapacitor, *J. Colloid Interface Sci.* **602** (2021) 721–731.
- [41] M. Song, Y. Zhou, X. Ren, J. Wan, Y. Du, G. Wu, F. Ma, Biowaste-based porous carbon for supercapacitor: the influence of preparation processes on structure and performance, *J. Colloid Interface Sci.* **535** (2019) 276–286.
- [42] B. Jia, Q. Mian, D. Wu, T. Wang, Heteroatoms self-doped porous carbon from cottonseed meal using K₂CO₃ as activator and DES electrolyte for supercapacitor with high energy density, *Materials Today Chemistry*, **24** (2022), 100828.
- [43] H. Liu, W. Chen, R. Zhang, C. Xu, X. Huang, H. Peng, C. Huo, M. Xu, Z. Miao, Bioinspired in situ self-catalyzing strategy towards graphene nanosheets with hierarchical structure derived from biomass for advanced supercapacitors, *Appl. Surf. Sci.* **566** (2021), 150692.
- [44] Y. Cao, K. Han, Z. Teng, J. Li, T. Ji, X. Li, J. Zhang, Optimized synergistic preparation of nitrogen-doped porous carbon derived from gasified carbon for supercapacitors, *J. Alloys Compd.* **860** (2021), 158385.
- [45] G. Zhong, M. Xu, S. Xu, X. Fu, W. Liao, Y. Xu, Green synthesis of iron and nitrogen co-doped porous carbon via pyrolysing lotus root as a high-performance electrocatalyst for oxygen reduction reaction, *Int. J. Energy Res.* **45** (2021) 10393–10408.
- [46] G. Zhong, H. Xie, Z. Xu, S. Xu, S. Xu, Z. Cai, X. Fu, W. Liao, R. Miao, Calcium chloride activation of mung bean: a low-cost, green route to N-doped porous carbon for supercapacitors, *ChemistrySelect*, **4** (2019) 3432–3439.
- [47] G. Zhong, Z. Meng, M. Xu, H. Xie, S. Xu, X. Fu, W. Liao, S. Zheng, Y. Xu, Self-nitrogen-doped porous carbon prepared via pyrolysis of grass-blade without additive for oxygen reduction reaction, *Diam. Relat. Mater.* **121** (2022), 108742.
- [48] Y. Zhou, X. Ren, M. Song, Y. Du, J. Wan, G. Wu, F. Ma, In-situ template cooperated with thiourea to prepare oxygen/nitrogen co-doped porous carbons with adjustable pore structure for supercapacitors, *Renew. Energy* **153** (2020) 1005–1015.
- [49] J. Shao, F. Ma, G. Wu, C. Dai, W. Geng, S. Song, J. Wan, In-situ MgO (CaCO₃) templating coupled with KOH activation strategy for high yield preparation of various porous carbons as supercapacitor electrode materials, *Chem. Eng. J.* **321** (2017) 301–313.
- [50] L. Yang, Y. Feng, M. Cao, J. Yao, Two-step preparation of hierarchical porous carbon from KOH-activated wood sawdust for supercapacitor, *Mater. Chem. Phys.* **238** (2019), 121956.

- [51] Y. Li, D. Zhang, Y. Zhang, J. He, Y. Wang, K. Wang, Y. Xu, H. Li, Y. Wang, Biomass-derived microporous carbon with large micropore size for high-performance supercapacitors, *J. Power Sources* 448 (2020), 227396.
- [52] Y. Tan, J. Ren, X. Li, L. He, C. Chen, H. Li, Highly graphitic porous carbon prepared via K_2FeO_4 -assisted KOH activation for supercapacitors, *New J. Chem.* 46 (2022) 14338–14345.
- [53] S. Huo, M. Liu, L. Wu, M. Liu, M. Xu, W. Ni, Y.-M. Yan, Synthesis of ultrathin and hierarchically porous carbon nanosheets based on interlayer-confined inorganic/organic coordination for high performance supercapacitors, *J. Power Sources* 414 (2019) 383–392.
- [54] J. Du, Y. Zhang, H. Lv, A. Chen, N/B-co-doped ordered mesoporous carbon spheres by ionothermal strategy for enhancing supercapacitor performance, *J. Colloid Interface Sci.* 587 (2021) 780–788.
- [55] W. Li, T. Wang, J. Guo, P. Liu, X. Yin, D. Wu, Organic resin based high surface area and N-enriched porous carbon nanosheets for supercapacitors, *Appl. Surf. Sci.* 599 (2022), 153885.
- [56] Z. Shen, J. Du, Y. Mo, A. Chen, Nanocomposites of reduced graphene oxide modified with mesoporous carbon layers anchored by hollow carbon spheres for energy storage, *Carbon*. 173 (2021) 22–30.
- [57] Y. Jiang, Z. He, X. Cui, Z. Liu, J. Wan, Y. Liu, F. Ma, Lamellar hierarchical porous carbon prepared from coal tar pitch through a lamellar hard template combined with the Precarbonization and activation method for supercapacitors, *ACS Appl. Energy Mater.* 5 (2022) 15199–15210.
- [58] L. Wan, J. Wang, L. Xie, Y. Sun, K. Li, Nitrogen-enriched hierarchically porous carbons prepared from Polybenzoxazine for high-performance supercapacitors, *ACS Appl. Mater. Interfaces* 6 (2014) 15583–15596.